ARTICLE IN PRESS

Available online at www.sciencedirect.com

ScienceDirect

Advances in Space Research xxx (xxxx) xxx

ADVANCES IN SPACE RESEARCH (a COSPAR publication)

www.elsevier.com/locate/asr

An onboard ultra-rapid orbit determination strategy for LEO satellite utilizing spaceborne GNSS data

Peng Luo [a,b], Yezhi Song [a,b,*], Xiaogong Hu [a,b], Qingfeng Wu [b,c], Jianhua Yang [a], Kai Li [a,b], Chengpan Tang [a,b], Changshao Chen [a,b]

[a] *Shanghai Astronomical Observatory, Chinese Academy of Sciences, Shanghai 200030, China*
[b] *University of Chinese Academy of Sciences, Beijing 100049, China*
[c] *Innovation Academy for Precision Measurement Science and Technology, CAS, Wuhan 430071, China*

Received 27 January 2026; received in revised form 25 May 2026; accepted 29 June 2026

Abstract

Precise orbit determination (POD) is essential for Low Earth Orbit (LEO) satellites supporting Earth science, remote sensing, communication, and navigation missions, for which the required real-time or near-real-time orbit accuracy ranges from meter level to centimeter level depending on the application. Emerging LEO positioning, navigation, and timing (LEO-PNT) missions further require short-term predicted orbits as the basis for onboard broadcast ephemeris generation. This study formulates the sequential least squares into an onboard adaptive sequential filtering strategy. Unlike the traditional sequential least squares, this adaptive sequential filtering strategy does not require long-arc accumulation and allows for frequent updates to the initial epoch, thus directly providing fast and stable predicted orbits to users immediately after the POD of each arc is completed. Validation using 48-h GNSS data from Sentinel-6 Michael Freilich (S6MF), Sentinel-3B (SE3B), and Swarm-A (SWMA) satellites with precise GNSS products demonstrates that the ultra-rapid POD consistency with independent precise reference orbits is better than 5 cm, with RMS values of 4.36 – 5.05 cm across all satellites. The predicted orbit consistency with respect to the reference orbits remains better than 20 cm in the user arc, with S6MF achieving < 10 cm at the 20th minute. The capability to support ground navigation is confirmed through Orbital User Range Error (OURE), with average OURE values of 4.69 cm, 6.59 cm, and 8.86 cm respectively. In GNSS-broadcast-ephemerides-limited scenario, the strategy maintains decimeter-level POD consistency and decimeter- to meter-level short-term prediction consistency, indicating its applicability boundary for autonomous onboard orbit determination and meter-level LEO applications.

Keywords: GNSS; LEO; Real-time orbit determination; Sequential least square; Onboard processing

1. Introduction

Low Earth Orbit (LEO) satellites, generally operating at altitudes below 2,000 km, are valuable platforms for geoscience, Remote Sensing (RS), and communication due to the shorter orbital periods and enhanced signal quality (Jin et al., 2021; Xiang et al., 2022; Laniewski et al., 2025). Precise orbits are essential for LEO satellites to support these services. For example, optical RS satellites require orbit accuracy better than 1 m. The Interferometric Synthetic Aperture Radar (InSAR) technology supported by Synthetic Aperture Radar (SAR) satellites requires an orbit accuracy of 5 cm for post-processing (Fernández et al., 2022) and 10 cm for real-time (RT)/near-real-time

* Corresponding author at: Shanghai Astronomical Observatory, Chinese Academy of Sciences, Shanghai 200030, China.
E-mail address: syz@shao.ac.cn (Y. Song).

https://doi.org/10.1016/j.asr.2026.06.114
0273-1177/

Please cite this article as: P. Luo, Y. Song, X. Hu et al., An onboard ultra-rapid orbit determination strategy for LEO satellite utilizing spaceborne GNSS data, Advances in Space Research, https://doi.org/10.1016/j.asr.2026.06.114

(NRT) processing (Fernández et al., 2024). Altimetry satellites require a radial orbital accuracy better than 3 cm (Montenbruck et al., 2021) for post-processing and 10 cm for RT/NRT processing (Fernández et al., 2024). In particular, the radial accuracy requirement of new-generation altimetry satellite Sentinel-6 Michael Freilich (S6MF) is 5 cm for NRT processing (Fernández et al., 2024).

Currently, spaceborne global navigation satellite system (GNSS) technology is widely employed for LEO satellites, achieving post-processing Precise Orbit Determination (POD) accuracy better than 1 cm (Mao et al., 2024). Beyond the traditional non-PNT applications mentioned above, such as Earth science, RS, and communication missions, emerging LEO constellations are increasingly considered for Positioning, Navigation, and Timing (PNT) services (Yang et al., 2024; Kunzi et al., 2026). Hereafter, PNT services based on LEO constellations are referred to as LEO-PNT services. Unlike traditional non-PNT LEO missions, which mainly use post-processing orbit products for their own mission objectives, LEO-PNT satellites act as navigation service providers and need to broadcast orbit and clock information to users through navigation messages. In this study, the orbit representation transmitted in the navigation message is referred to as the broadcast ephemeris (BRDC). For ground users, the BRDC is required to compute the LEO satellite position at the signal transmission time and to model LEO-to-user ranging observations for positioning. For LEO-PNT services, performing Real-Time Precise Orbit Determination (RTPOD) alone is not sufficient. The BRDC should represent the satellite trajectory over a future validity interval, and its orbit parameters are generally fitted from predicted satellite positions. Therefore, onboard POD results need to be followed by short-term orbit prediction before the BRDC can be generated. Recent studies have commonly considered prediction and fitting intervals of $10-20$ min for LEO-PNT BRDC generation, and have shown that the prediction error is usually the dominant error source compared with the ephemeris fitting error (Kunzi et al., 2026). Thus, stable short-term orbit prediction is a key requirement for onboard LEO-PNT BRDC generation.

Significant progress has been made in LEO RTPOD based on the extended Kalman filter (EKF) and its variants. For example, Wang et al. (2023) conducted RTPOD experiments using spaceborne Global Positioning System (GPS) data from the FY-3C satellite and state-space representation (SSR) products provided by the Centre National d'Etudes Spatiales (CNES), achieving an orbit accuracy better than 10 cm. Li (2024) performed RTPOD experiments for S6MF using CNES SSR products and a square-root information filter (SRIF), improving the ambiguity-fixed 3D orbit accuracy to 3.61 cm, by about 30% compared with the ambiguity-float solution. Montenbruck et al. (2022) also assessed GNSS-based real-time navigation for the same satellite and achieved an accuracy better than 10 cm by combining GPS and Galileo observations, even when using GNSS broadcast ephemerides only. More recently, Kunzi et al. (2026) evaluated EKF-based RTPOD and short-term prediction for LEO-PNT BRDC generation. These studies demonstrate the maturity of EKF-based RTPOD, while also showing that prediction performance remains sensitive to force-model errors, dynamic-parameter estimation, and atmospheric drag, especially for low-altitude LEO satellites. For onboard LEO-PNT BRDC generation, the processing strategy should therefore consider both RTPOD and short-term prediction stability.

This requirement is conceptually similar to the traditional GNSS broadcast ephemeris generation procedure, in which POD results are first propagated to generate predicted orbits and then fitted into broadcast ephemeris parameters. For example, the broadcast ephemerides of the BeiDou Navigation Satellite System (BDS) are generated by fitting predicted orbits derived from Batch Least Squares (BLSQ)-based POD using ground-satellite link and inter-satellite link observations (Chen et al., 2022). GNSS autonomous navigation follows a similar procedure, in which broadcast ephemeris parameters are generated from predicted orbits after POD, either through centralized or distributed EKF-based processing strategies (Mao et al., 2015). Li et al. (2019) further improved multi-GNSS ultra-rapid product generation by implementing multi-threaded parallel processing. Using a 2-day BLSQ POD arc, they achieved hourly five-constellation ultra-rapid orbit updates to support real-time precise point positioning (PPP).

However, directly applying such long-arc, ground-based product generation strategies to LEO onboard processing is impractical. Compared with GNSS satellites, LEO satellites have much shorter orbital periods and experience stronger perturbations, especially atmospheric drag and high-degree gravity field effects. As a result, their prediction errors accumulate more rapidly, and more frequent orbit updates are required. Meanwhile, onboard processors have limited computing and storage resources, while ground-based processing may suffer from data transmission delays and link-dependency risks. Therefore, onboard LEO orbit determination and short-term prediction require a processing strategy that can retain the dynamic fitting capability of arc-based orbit determination while avoiding the computational burden of long-arc BLSQ processing.

To address the conflict between the need for dynamic fitting (for prediction stability) and the constraints of onboard computing resources, the Sequential Least Squares (SLSQ) method offers a robust solution. Originally proposed by Beutler et al. (1996) to efficiently combine normal equations (NEQ) for GNSS orbits, this method maintains the mathematical equivalence to batch processing while significantly reducing CPU load and memory usage. While theoretically equivalent to the Kalman filter under linear assumptions, the SLSQ approach is distinct in its handling of NEQ, making it particularly suitable for arc-based processing.

Zhao et al. (2018) and Fu et al. (2019) have successfully applied sliding-window variants of this method to GNSS orbit determination and clock estimation. Nevertheless, existing applications of SLSQ for GNSS typically rely on long data arcs (e.g., 48 h) to ensure stability, benefiting from abundant ground computing resources. In contrast, the constrained onboard environment of LEO satellites necessitates significantly shorter arc lengths. Consequently, adapting the SLSQ method into a general filtering framework suitable for ultra-rapid LEO prediction remains unexplored.

In this study, we reformulate the SLSQ method into an onboard adaptive sequential filtering strategy for LEO ultra-rapid orbit determination and short-term prediction. The method retains the arc-wise dynamic fitting capability of least-squares orbit determination, while using sequential NEQ propagation to avoid long-arc accumulation and reduce storage requirements. By frequently updating the initial epoch, the strategy can generate short-term prediction orbit products immediately after each POD arc, making it suitable for onboard rapid BRDC generation under limited computing resources. Since publicly available spaceborne GNSS observations from operational LEO-PNT satellites are not yet available, we validate this strategy using spaceborne GNSS data from S6MF, Sentinel-3B (SE3B), and Swarm-A (SWMA) satellites. Computational experiments are conducted under two scenarios, using precise GNSS products and GNSS broadcast ephemerides only, to evaluate the performance of both RTPOD and short-term orbit prediction for LEO-PNT BRDC generation.

2. Methodology

We first present the model of spaceborne GNSS observations, method of NEQ formation with these observations and clock offset elimination for NEQ. Then, the formulation of the adaptive sequential least squares filter which were used in this paper will be introduced.

2.1. Observation model

The pseudorange and carrier phase observations from an onboard receiver r equipped on a LEO satellite to GNSS satellite S at frequency j can be expressed as (Li, 2024):

$$\begin{cases} P_{r,j}^{s} = \rho_r^s + c\delta t_r - c\delta t_s + \delta\rho_{ion,j} + \delta\rho_{rel} + \delta\rho_{pco,j} + \delta\rho_{pco,j}^{s} + \varepsilon_P \\ L_{r,j}^{s} = \rho_r^s + c\delta t_r - c\delta t_s - \delta\rho_{ion,j} + \delta\rho_{rel} + \delta\rho_{pco,j} + \delta\rho_{pco,j}^{s} + \lambda_j N_j^s + \varepsilon_L \end{cases} \tag{1}$$

where $P_{r,j}^{s}$ and $L_{r,j}^{s}$ are the pseudorange and carrier phase observations for receiver r, respectively; ρ_r^s denotes the geometric distance from the LEO satellite to the GNSS satellite S; c denotes the speed of light; δt_r and δt_s are clock offset of onboard receiver and GNSS satellite S, respectively; $\delta\rho_{ion,j}$ is the ionospheric delay; $\delta\rho_{rel}$ is the general relativity correction; $\delta\rho_{pco,j}$ and $\delta\rho_{pco,j}^{s}$ denote the antenna Phase Center Offset (PCO) correction of the LEO satellite and GNSS satellite S, respectively; λ_j is the wavelength; N_j^s is ambiguity (unit: cycle); ε_P and ε_L are both noises of the pseudo-range and carrier phase observations, respectively.

The ionospheric delay is one of main error sources for GNSS observations. In order to eliminate the effect of ionospheric delay, a typical ionosphere-free (IF) combination for dual-frequency pseudo-range and carrier phase observation can be derived (Li, 2024):

$$\begin{cases} P_{r,IF}^{s} = \frac{f_i^2}{f_i^2 - f_j^2} \cdot P_{r,i}^{s} - \frac{f_j^2}{f_i^2 - f_j^2} \cdot P_{r,j}^{s} \\ L_{r,IF}^{s} = \frac{f_i^2}{f_i^2 - f_j^2} \cdot L_{r,i}^{s} - \frac{f_j^2}{f_i^2 - f_j^2} \cdot L_{r,j}^{s} \end{cases} \tag{2}$$

where $P_{r,IF}^{s}$ and $L_{r,IF}^{s}$ are the IF pseudorange and carrier phase observations, respectively; i and j denote the frequency number; f_i is the i^{th} frequency.

2.2. NEQ formation with spaceborne GNSS observations

The equation of motion for a satellite in LEO can be expressed as (Tapley et al., 2004):

$$\ddot{\mathbf{r}} = -GM\frac{\mathbf{r}}{r^3} + \mathbf{f}(\mathbf{r}, \dot{\mathbf{r}}, \mathbf{p}, t) \tag{3}$$

where $\mathbf{r}, \dot{\mathbf{r}}$ and $\ddot{\mathbf{r}}$ are the position, velocity, and acceleration of the satellite's center of mass respectively. $\mathbf{p}$ is the vector of dynamic orbit parameters, for instance, atmospheric drag factor, solar radiation factor and empirical accelerations, etc.

The perturbation acceleration acting on the satellite, denoted as $\mathbf{f}$, is the cumulative effect of various perturbations including n-body perturbation, earth non-spherical gravity field, earth's tidal forces, solar radiation pressure, Earth radiation pressure, relativistic effects, etc.

Let $\mathbf{X} = (\mathbf{r}, \dot{\mathbf{r}}, \mathbf{p})^T$, then the state equation and initial state of the satellite can be expressed as:

$$\begin{cases} \dot{\mathbf{X}} = \mathbf{F}(\mathbf{X}, t) = (\dot{\mathbf{r}}, \ddot{\mathbf{r}}, \dot{\mathbf{p}})^T \\ \mathbf{X}|_{t_0} = \mathbf{X}_0 \end{cases} \tag{4}$$

Assume a state vector $\mathbf{X}_0$ at the initial epoch is known, and then the initial state $\mathbf{X}^*$ at epoch t can be obtained through the integration of Eq. (4). The linear expansion of Eq. (4) leads to:

$$\dot{\mathbf{X}} = \dot{\mathbf{X}}^* + \frac{\partial \mathbf{F}}{\partial \mathbf{X}}|_{\mathbf{X}^*}(\mathbf{X} - \mathbf{X}^*) \tag{5}$$

Let $\mathbf{A} = \frac{\partial \mathbf{F}}{\partial \mathbf{X}}|_{\mathbf{X}^*}$, $\mathbf{x} = \mathbf{X} - \mathbf{X}^*$, then the Eq. (5) can be expressed as:

$$\dot{\mathbf{x}} = \mathbf{A}\mathbf{x} \tag{6}$$

The general solution of Eq. (6) can be expressed as:

$$\mathbf{x} = \mathbf{\Psi}(t, t_0)\mathbf{x}_0 \tag{7}$$

where the $\mathbf{\Psi}(t, t_0)$ is a state transition matrix. The correction of the initial state is denoted as $\mathbf{x}_0$.

The spaceborne GNSS IF observations at i^{th} epoch can be expressed as following, after combining Eq. (7):

$$\begin{cases} \mathbf{y}_i = \begin{bmatrix} \mathbf{H}_{G,i} & \mathbf{H}_{T,i} \end{bmatrix} \begin{bmatrix} \mathbf{z} \\ \delta t_i \end{bmatrix} + \boldsymbol{\varepsilon}_i \\ \mathbf{H}_{G,i} = \begin{bmatrix} \frac{\partial \mathbf{y}_i}{\partial \mathbf{x}_i} \boldsymbol{\Psi}(t_i, t_0) & \frac{\partial \mathbf{y}_i}{\partial \delta AMB_{IF,1}} & \cdots & \frac{\partial \mathbf{y}_i}{\partial \delta AMB_{IF,m}} \end{bmatrix} \\ \mathbf{H}_{T,i} = \frac{\partial \mathbf{y}_i}{\partial \delta t_i} \\ \mathbf{z} = \begin{bmatrix} \mathbf{x}_0^T & \delta AMB_{IF,1} & \cdots & \delta AMB_{IF,m} \end{bmatrix}^T \end{cases} \tag{8}$$

where $\mathbf{z}$ denotes the correction vector of global estimated parameters (For example, orbital parameters, IF ambiguities, etc.); $\delta AMB_{IF,j}$ is $j^{th}(1 \leqslant j \leqslant m, m$ is the total number of ambiguities) IF ambiguity's correction (unit: meter); δt_i denotes the clock offset; $\mathbf{H}_{G,i}$ and $\mathbf{H}_{T,i}$ are design matrices for $\mathbf{z}$ and δt_i, respectively; $\boldsymbol{\varepsilon}_i$ is noise of $\mathbf{y}_i$; and the covariance matrix of $\mathbf{y}_i$ is $\mathbf{D}_i$. The NEQ for $\mathbf{z}$ and δt_i can be derived by combining Eq. (7) and Eq. (8), after employing the least square method. Written as:

$$\begin{bmatrix} \mathbf{N}_{GG,i} & \mathbf{N}_{GT,i} \\ \mathbf{N}_{TG,i} & \mathbf{N}_{TT,i} \end{bmatrix} \begin{bmatrix} \hat{\mathbf{z}} \\ \delta t_i \end{bmatrix} = \begin{bmatrix} \mathbf{W}_{G,i} \\ \mathbf{W}_{T,i} \end{bmatrix} \tag{9}$$

$$\begin{cases} \mathbf{N}_{GG,i} = \mathbf{H}_{G,i}^T \mathbf{D}_i^{-1} \mathbf{H}_{G,i} \\ \mathbf{N}_{GT,i} = \mathbf{H}_{G,i}^T \mathbf{D}_i^{-1} \mathbf{H}_{T,i} = \mathbf{N}_{TG,i}^T \\ \mathbf{N}_{TT,i} = \mathbf{H}_{T,i}^T \mathbf{D}_i^{-1} \mathbf{H}_{T,i} \\ \mathbf{W}_{G,i} = \mathbf{H}_{G,i}^T \mathbf{D}_i^{-1} \cdot \mathbf{y}_i \\ \mathbf{W}_{T,i} = \mathbf{H}_{T,i}^T \mathbf{D}_i^{-1} \cdot \mathbf{y}_i \end{cases} \tag{10}$$

After combining all epoch-wised NEQs, the final NEQ can be written as:

$$\mathbf{N}_{bb} \begin{bmatrix} \mathbf{z}^T & \delta t_1 & \cdots & \delta t_n \end{bmatrix}^T = \mathbf{W}_y \tag{11}$$

where

$$\mathbf{N}_{bb} = \begin{bmatrix} \sum \mathbf{N}_{GG,i} & \mathbf{N}_{GT,1} & \cdots & \mathbf{N}_{GT,n} \\ \mathbf{N}_{TG,1} & \mathbf{N}_{TT,1} & \ldots & 0 \\ \vdots & \vdots & \ddots & \vdots \\ \mathbf{N}_{TG,n} & 0 & \cdots & \mathbf{N}_{TT,n} \end{bmatrix} \tag{12}$$
$$\mathbf{W}_y = \begin{bmatrix} \sum \mathbf{W}_{G,i}^T & \mathbf{W}_{T,1}^T & \cdots & \mathbf{W}_{T,n}^T \end{bmatrix}^T$$

2.3. Clock offset elimination for NEQ

It should be noted that Eq. (11) contains $n_{orb} + n_{amb} + n_{clk}$ parameters to be estimated, including n_{orb} orbital parameters, n_{amb} ambiguities, and n_{clk} clock offsets, where the number of observation epochs is $n(n = n_{clk})$. Solving Eq. (11) would require substantial storage space and computational time. According to Liao et al. (2024), the clock offset parameters can be treated as local parameters and can be eliminated during the formation of the NEQ. After elimination, the NEQ can be written as:

$$\mathbf{N} \cdot \hat{\mathbf{z}} = \mathbf{W} \tag{13}$$

where

$$\begin{aligned} \mathbf{N} &= \sum \left(\mathbf{N}_{GG,i} - \mathbf{N}_{GT,i} (\mathbf{N}_{TT,i})^{-1} \mathbf{N}_{TG,i} \right) \\ \mathbf{W} &= \sum \left(\mathbf{W}_{G,i} - \mathbf{N}_{GT,i} (\mathbf{N}_{TT,i})^{-1} \mathbf{W}_{T,i} \right) \end{aligned} \tag{14}$$

Eq. (13) greatly reduces the dimensionality of the origin NEQ, and its solving result is equal to that of Eq. (11). If the epoch-wised clock offsets are needed, they can also be easily resolved(Liao et al., 2024).

2.4. Formulation of the adaptive sequential least squares filter

The traditional SLSQ strategies for precise orbit determination typically do not require frequent updates to the initial epoch. For instance, the NEQ stacking method proposed by Beutler et al. (1996) combines multiple one-day arcs to generate three-day solutions, which is equivalent to updating the initial epoch every 24 h. Similarly, Zhao et al. (2018) updated the initial epoch every 30 min in their GNSS POD implementation. However, this is not suitable for onboard platforms with limited computing resources and storage capacity. This is because updating the initial epoch less frequently requires longer orbital dynamic integration, which significantly increases the computational burden. To address this, drawing on the data processing strategy proposed by Ge et al. (2006), we formulate the SLSQ into an adaptive sequential filtering framework. This approach maintains solution accuracy even with frequent updates to the initial epoch and is formally equivalent to a Kalman filter, comprising both measurement update and time update steps.

2.4.1. Measure updates

Assuming that the prior estimated parameters at arc k can be expressed as

$$\overline{\mathbf{Z}}_k = \begin{bmatrix} \overline{\mathbf{Z}}_{k,dyn}^T & \overline{\mathbf{Z}}_{k,ndyn}^T \end{bmatrix}^T \tag{15}$$

where the $\mathbf{Z}_{k,dyn}$ denotes the time-varying parameter such as orbit parameters; $\mathbf{Z}_{k,ndyn}$ denotes the non-time-varying parameter such as ambiguities. The correction to $\overline{\mathbf{Z}}_k$ can be written as $\hat{\mathbf{z}}_k = \begin{bmatrix} \hat{\mathbf{z}}_{dyn,k}^T & \hat{\mathbf{z}}_{ndyn,k}^T \end{bmatrix}^T$, and it's prior NEQ is given by:

$$\overline{\mathbf{N}}_k \hat{\mathbf{z}}_k = \bar{\mathbf{w}}_k \tag{16}$$

The NEQ can be built with only observations in this arc according to Eq. (13), which can be expressed as:

$$\mathbf{N}_k \hat{\mathbf{z}}_k = \mathbf{w}_k \tag{17}$$

In order to improve the stability of the solution, we refer to the adaptive filtering theory proposed by Yang et al. (2013), and the final NEQ in iteration form of this arc can be expressed combining Eq. (16) and Eq. (17) as:

$$\left(\mathbf{N}_k + \alpha \overline{\mathbf{N}}_k \right) \hat{\mathbf{z}}_k = \mathbf{w}_k + \alpha \left(\bar{\mathbf{w}}_k - \overline{\mathbf{N}}_k \bar{\mathbf{z}}_k \right) \tag{18}$$

where the $\alpha (0 < \alpha \leqslant 1)$ denotes the adaptive factor; $\hat{\mathbf{z}}_k$ denotes the parameters' correction; $\bar{\mathbf{z}}_k$ denotes the prior parameters' correction. Generally, when the observation system exhibits significant nonlinearity, Eq. (18) is typically solved iteratively to obtain the optimal estimate. The iterative form is expressed as:

$$(\mathbf{N}_k + \alpha \overline{\mathbf{N}}_k)\hat{\mathbf{z}}_k^t = \mathbf{w}_k + \alpha\left(\bar{\mathbf{w}}_k - \overline{\mathbf{N}}_k \sum_{n=0}^{t-1} \hat{\mathbf{z}}_k^n\right) \tag{19}$$

where $\hat{\mathbf{z}}_k^t$ denotes the parameter correction at the tth iteration. The adaptive factor α controls the contribution of the prior NEQ in Eq. (18). When $\alpha = 1$, the contribution of the prior NEQ $\overline{\mathbf{N}}_k$ is fully retained. When $\alpha < 1$, the prior NEQ $\overline{\mathbf{N}}_k$ is weakened, and the current-arc observations are allowed to contribute more strongly to the solution. Since the prior normal matrix $\overline{\mathbf{N}}_k$ represents inverse covariance information, reducing α is equivalent to inflating the prior covariance, which plays a role similar to covariance inflation or fading-memory weighting in adaptive Kalman filtering. In this paper, the following function is used to determine α:

$$\alpha = \begin{cases} 1, & \Delta x < c \\ c/\Delta x, & \Delta x \geqslant c \end{cases} \tag{20}$$

where c is an empirical constant, which is usually set to $1.5 - 2.0$ based on experience (Yang and Gao, 2006); Δx denotes the normalized difference between the solution and prior values. When only the position component $\mathbf{pos}_k = (X, Y, Z)^{\mathrm{T}}$ is considered, Δx can be expressed as follows:

$$\Delta x = \sqrt{\frac{\Delta \mathbf{pos}_k^{\mathrm{T}} \Delta \mathbf{pos}_k}{\mathrm{tr}(\mathbf{cov}_k(\mathbf{pos}))}} \tag{21}$$

where $\Delta \mathbf{pos}_k$ denotes the position difference between the solution and prior values at the initial epoch; $\mathbf{cov}_k(\mathbf{pos})$ denotes the prior covariance matrix of the position at the initial epoch; and $\mathrm{tr}(\mathbf{cov}_k(\mathbf{pos}))$ represents its trace. If $\Delta x < c$, the prior information is regarded as consistent with the current observations and α is set to 1. Otherwise, α decreases as Δx increases, thereby reducing the influence of the prior NEQ and improving the adaptability of the solution to the current observation arc.

After the iterative solution and convergence of Eq. (19), the new parameters will be estimated and written as $\widehat{\mathbf{Z}}_k \sim N\left(\overline{\mathbf{Z}}_k + \hat{\mathbf{z}}_k, \widehat{\mathbf{N}}_k^{-1} \cdot \hat{\sigma}_0^2\right)$, and the post-estimated NEQ can be expressed as:

$$\widehat{\mathbf{N}}_k \hat{\mathbf{z}}_k = \widehat{\mathbf{w}}_k \tag{22}$$

Which can be also written as:

$$\begin{bmatrix} \widehat{\mathbf{N}}_{k,dyn} & \widehat{\mathbf{N}}_{k,\mathrm{cov}} \\ \widehat{\mathbf{N}}_{k,\mathrm{cov}}^T & \widehat{\mathbf{N}}_{k,ndyn} \end{bmatrix} \begin{bmatrix} \hat{\mathbf{z}}_{dyn,k} \\ \hat{\mathbf{z}}_{ndyn,k} \end{bmatrix} = \begin{bmatrix} \widehat{\mathbf{w}}_{k,dyn} \\ \widehat{\mathbf{w}}_{k,ndyn} \end{bmatrix} \tag{23}$$

2.4.2. Time updates

For the current arc $k+1$, the time-varying parameters can be updated according to Eq. (3) to obtain the a priori estimation parameter $\overline{\mathbf{Z}}_{k+1} = \begin{bmatrix} \overline{\mathbf{Z}}_{k+1,dyn}^T & \overline{\mathbf{Z}}_{k+1,ndyn}^T \end{bmatrix}^T$ for current arc. Meanwhile, the prediction equation for the time-varying parameter correction $\bar{\mathbf{z}}_{k+1,dyn}$ can also be written according to Eq. (7):

$$\bar{\mathbf{z}}_{k+1,dyn} = \mathbf{\Psi}(k+1,k)\hat{\mathbf{z}}_{k,dyn} + \boldsymbol{\omega}, \quad \boldsymbol{\omega} \sim N(\mathbf{0}, \mathbf{Q}_w) \tag{24}$$

where $\boldsymbol{\omega}$ denotes the processing noise; $\mathbf{Q}_w$ denotes the covariance matrix of $\boldsymbol{\omega}$. Referring to Ge et al. (2006), Eq. (24) can be treated as a pseudo-observation and associated with Eq. (23) to obtain the total NEQ:

$$\begin{bmatrix} \widehat{\mathbf{N}}_{k,dyn} + \mathbf{\Psi}^T \mathbf{Q}_w^{-1} \mathbf{\Psi} & -\mathbf{\Psi}^T \mathbf{Q}_w^{-1} & \widehat{\mathbf{N}}_{k,\mathrm{cov}} \\ -\mathbf{Q}_w^{-1} \mathbf{\Psi} & \mathbf{Q}_w^{-1} & \mathbf{0} \\ \widehat{\mathbf{N}}_{k,\mathrm{cov}}^T & \mathbf{0} & \widehat{\mathbf{N}}_{k,ndyn} \end{bmatrix} \begin{bmatrix} \hat{\mathbf{z}}_{k,dyn} \\ \bar{\mathbf{z}}_{k+1,dyn} \\ \bar{\mathbf{z}}_{k+1,ndyn} \end{bmatrix} = \begin{bmatrix} \widehat{\mathbf{w}}_{k,dyn} \\ \mathbf{0} \\ \widehat{\mathbf{w}}_{k,ndyn} \end{bmatrix} \tag{25}$$

To facilitate the subsequent derivation, we express the above equation in the following concise form:

$$\begin{bmatrix} \mathbf{N}_{11} & \mathbf{N}_{12} & \mathbf{N}_{13} \\ \mathbf{N}_{21} & \mathbf{N}_{22} & \mathbf{0} \\ \mathbf{N}_{31} & \mathbf{0} & \mathbf{N}_{33} \end{bmatrix} \begin{bmatrix} \hat{\mathbf{z}}_{k,dyn} \\ \bar{\mathbf{z}}_{k+1,dyn} \\ \bar{\mathbf{z}}_{k+1,ndyn} \end{bmatrix} = \begin{bmatrix} \widehat{\mathbf{w}}_{k,dyn} \\ \mathbf{0} \\ \widehat{\mathbf{w}}_{k,ndyn} \end{bmatrix} \tag{26}$$

In fact, we only concern about $\bar{\mathbf{z}}_{k+1,dyn}$ and $\bar{\mathbf{z}}_{k+1,ndyn}$, and the $\hat{\mathbf{z}}_{k,dyn}$ is treated as outdated parameters which should be eliminated. Following the approach described by Ge et al. (2006), we eliminate $\hat{\mathbf{z}}_{k,dyn}$, result in the priori NEQ for the estimated parameters in this arc, given as follows:

$$\begin{bmatrix} \mathbf{N}_{22} - \mathbf{N}_{21}\mathbf{N}_{11}^{-1}\mathbf{N}_{12} & -\mathbf{N}_{21}\mathbf{N}_{11}^{-1}\mathbf{N}_{13} \\ -\mathbf{N}_{31}\mathbf{N}_{11}^{-1}\mathbf{N}_{12} & \mathbf{N}_{33} - \mathbf{N}_{31}\mathbf{N}_{11}^{-1}\mathbf{N}_{13} \end{bmatrix} \begin{bmatrix} \bar{\mathbf{z}}_{k+1,dyn} \\ \bar{\mathbf{z}}_{k+1,ndyn} \end{bmatrix} = \begin{bmatrix} -\mathbf{N}_{21}\mathbf{N}_{11}^{-1}\widehat{\mathbf{w}}_{k,dyn} \\ \widehat{\mathbf{w}}_{k,ndyn} - \mathbf{N}_{31}\mathbf{N}_{11}^{-1}\widehat{\mathbf{w}}_{k,dyn} \end{bmatrix} \tag{27}$$

2.4.3. Initial step

In particular, when $k = 0$, if only the priori estimated parameter $\overline{\mathbf{Z}}_0 = \begin{bmatrix} \overline{\mathbf{Z}}_{0,dyn}^T & \overline{\mathbf{Z}}_{0,ndyn}^T \end{bmatrix}^T$, and its correction $\hat{\mathbf{z}}_0 = \begin{bmatrix} \hat{\mathbf{z}}_{0,dyn}^T & \hat{\mathbf{z}}_{0,ndyn}^T \end{bmatrix}^T$ satisfy the following relation:

$$\overline{\mathbf{Z}}_0 + \hat{\mathbf{z}}_0 = \widetilde{\mathbf{Z}}_0 + \boldsymbol{\varepsilon}_z \quad \boldsymbol{\varepsilon}_z \sim N(\mathbf{0}, \mathbf{D}_0) \tag{28}$$

where $\widetilde{\mathbf{Z}}_0$ denotes the true value of initial orbit in this arc; $\boldsymbol{\varepsilon}_z$ denotes the noise associated with $\overline{\mathbf{Z}}_0$; $\mathbf{D}_0$ denotes the priori covariance matrix of $\overline{\mathbf{Z}}_0$. The priori NEQ can be written as:

$$\mathbf{D}_0^{-1}\hat{\mathbf{z}}_0 = \mathbf{0} \tag{29}$$

Subsequent measure updates and time updates can be performed based on this priori NEQ.

3. Onboard ultra-rapid orbit determination strategy

Based on this adaptive sequential filtering algorithms, we have independently developed POD software in C99, named the Spacecraft Orbit Determination Analyzer (SODA). This software supports both post-processing POD and RTPOD for LEO satellites. The RTPOD workflow is shown in Fig. 1.

As seen in Fig. 1, this RTPOD procedure is similar to the traditional BLSQ. Meanwhile, a calculation delay needs to be considered at each POD initialization, as we reuse the historical observations during the real-time processing to maintain estimation accuracy, similar to the method of Zhao et al. (2018). Thus, our POD process functions as a sliding-window BLSQ, representing an ultra-rapid processing strategy.

To make an optimal balance between onboard computing efficiency and orbital prediction stability, we empirically determined the configuration to be a 30-min historical observation window with a 5-min calculation delay. Consequently, the prediction orbit product is released at a 5-min interval. Note that these settings can be modified to adapt to different onboard computers and mission requirements. Fig. 2 illustrates the delay and updating sequence of this real-time processing.

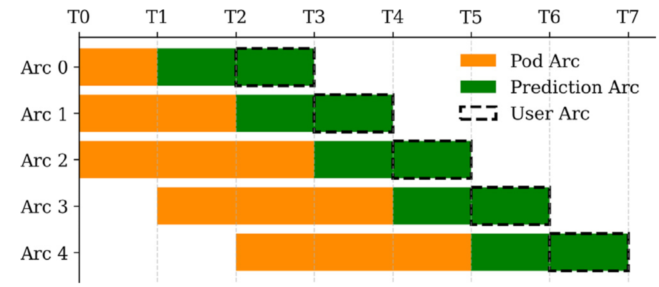

Fig. 2. The calculation delay and arc updating of real-time processing. The orange part is only used for orbit determination called pod arc; the green part is the orbital prediction after POD of each arc, and only the part framed by the dotted line will be provided to user for their application, which is called user arc; the period between the pod arc and the user arc is the calculation delay.

4. Dataset and model description

For controlled validation and direct comparison with independent precise reference orbits, we replay 48 h of real spaceborne GPS observations from Sentinel-6 Michael Freilich (S6MF), Sentinel-3B (SE3B), and Swarm-A (SWMA) on the ground to simulate the real-time onboard processing sequence. These satellites operate at 3 typical altitudes — 1336 km, 814.5 km and 462 km — allowing the assessment of RTPOD and orbit prediction performance under a uniform processing strategy across different orbital regimes. More details of these satellites can be found in Table 1.

To simulate realistic scenarios, both BRDC and final GNSS products provided by the Center for Orbit Determination in Europe (CODE) are used separately in the calculation. The POD and prediction performance for S6MF and SE3B is evaluated by comparison with post-processed precise orbits conforming to the Precise Orbit Ephemeris-F (POE-F) standards provided by CNES (ftp://ftp.ids-doris.org/pub/ids/data/POD_configuration_POEF.pdf). For SWMA, the RDPOD products from the European Space Agency (ESA) serve as the reference. Since these reference orbit products have substantially higher accuracy than the orbit differences reported in this study, they are used as reliable references for performance evaluation.

Limited by the onboard computing resources, gravitational force model simplification is usually required. A 90 × 90 EIGEN_GL04C Earth gravity field model is adopted in our study, and all the earth tides including solid earth tide, ocean tide (20 × 20) and pole tides are considered. The macro-models of these satellites provided by ESA are used to describe the geometric and physical properties of satellite surfaces for the calculation of solar radiation pressure and atmospheric drag. Finally, the empirical acceleration parameters with sine/cosine terms are adopted and estimated for the along and cross-track directions to compensate the unmodeled perturbations for each arc. As our parameter estimation is no longer the epoch-wised, the Krogh-Shampine-Gordon (KSG) multiple-step integrator (Zhang and Liu, 1998) is used during orbital integration, which greatly improves the calculation efficiency.

In our estimation strategy, POD is performed every 5 min, with each arc utilizing only the observation data from the preceding 30 min. After each POD, we provide

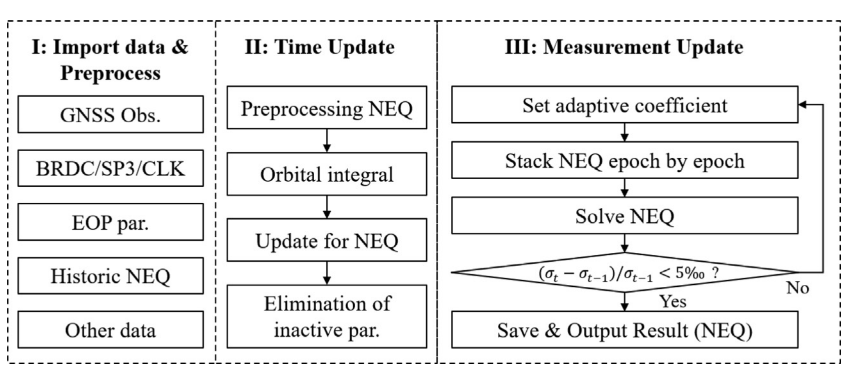

Fig. 1. The RTPOD procedure of SODA, where σ_t denotes the Unit Weight Error (UWE) of observations in t^{th} iteration.

Table 1
Information of LEO satellites and their spaceborne GPS observations.

	S6MF	SE3B	SWMA
Altitude	1336 km	814.5 km	462 km
Inclination	66 deg	98.65 deg	87.35 deg
Launch date	21 November 2020	25 April 2018	22 November 2013
Obs. type	C1C/C2L/L1C/L2L	C1W/C2W/L1C/L2W	
Obs. Duration	From 1 September 2021 to 3 September 2021		

an additional 20 min of predicted orbit to users for their applications. Other information about models adopted for POD in this paper and the parameter estimation strategy for each arc are presented in Table 2.

To verify the onboard computational feasibility, the same estimation strategy was tested on an embedded platform using 24 h of spaceborne GNSS data from SWMA. The maximum computation time per POD arc was 70.49 s, which is well below the 5-min update interval adopted in this study, and the corresponding delay illustration of each arc is shown in Fig. 3. Given these results, the subsequent validation focuses on the consistency of the POD solutions and orbital prediction, without further consideration of computational delays.

Table 2
models and the parameter estimation strategy.

Items	**Models & Description**
Measurement Model	
GNSS orbit and clocks	Broadcast ephemeris/ CODE final products
GNSS satellite antenna	Igs14.atx
Observations	Dual-frequency IF combination
Sampling	30 s
Receiver antenna	PCO is considered only (In-flight calibration)
LEO satellite attitude	Quaternions (measured)
Carrier phase wind-up	Applied
Outlier observation process	3σ criterion
Weight function	$\sin^2(z), z$ is the elevation angle of the GNSS satellite
Parameter estimation	Adaptive Sequential Filter
Dynamic model	
Earth orientation parameters	EOP IERS Bulletin A
Gravitational forces	EIGEN _ GL04C (90 × 90) (Förste et al., 2006); N-body gravity: DE421 (Folkner et al., 2009)
Solid earth tide	IERS2010(Petit and Luzum, 2010)
Ocean tide	FES2004(Lyard et al., 2006), 20 × 20
Pole tides	IERS2010(Petit and Luzum, 2010)
General relativity	IERS2010 (Petit and Luzum, 2010)
Solar radiation pressure	Spacecraft macro-model(Montenbruck et al., 2015)
Atmospheric drag	NRLMSIS-00 (Picone et al., 2002)
Empirical accelerations	Consider the parameters of Ca, Sa, Cc and Sc for the along- and cross-track directions (cosine/sine) only
Integrator	KSG (Zhang and Liu, 1998)
Integral step	15 s
Solved parameters	
Orbit parameters	Position and velocity at the initial epoch of each arc
Receiver clock offsets	Estimated for each epoch
Ambiguities	Estimate IF ambiguities
Solar radiation factor	1 factor
Atmospheric drag factor	1 factor
Empirical accelerations	1 group for each arc
Arc updating interval	5 min
Arc length	30 min
User arc length	20 min

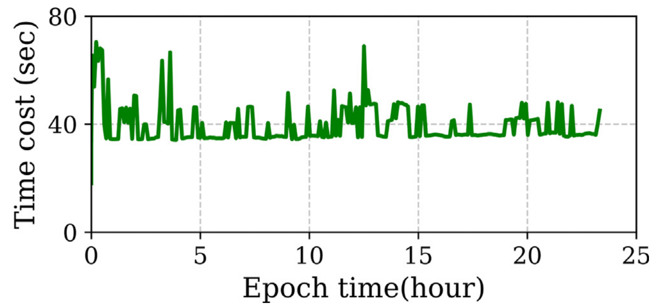

Fig. 3. The time cost of each pod arc on embedded platform for testing. (Platform info: SOC: ZYNQ7045; CPU: ARM Cortex-A9; Main frequency: 800 MHz; DDR: 1 GB).

5. Results and analysis

5.1. POD performance based on final products

In this section, we firstly perform a simple evaluation of the observation. Subsequently, comparisons are carried out between the reference orbits and the POD results based on CODE final products.

Fig. 4 shows the epoch-wise number of satellites and Position Dilution of Precision (PDOP) of S6MF, SE3B and SWMA. As our software allows to select only one couple of signals per constellation currently, we only prefer the L1C/L2L signals for S6MF. This selection discards the GPS Block IIR satellites, which do not broadcast on L2L, resulting in S6MF having a lower mean number of satellites (6.3 per epoch) compared to SE3B (7.5 per epoch) and SWMA(7.5 per epoch). Additionally, SE3B exhibits the best PDOP among the three satellites, with an average PDOP of 4.831 during this period, whereas the averages for SWMA and S6MF are 5.509 and 5.455, respectively.

After processing a total of 556 POD sessions for each satellite, all the IF phase weighted Root-Mean-Square

Table 3
Weighted-RMS of residuals for S6MF, SE3B and SWMA (unit: cm).

	S6MF	SE3B	SWMA
IF range	57.63	21.99	23.49
IF phase	0.44	0.47	0.45

(RMS) values are better than 5 mm, as shown in Table 3. Although the sliding window advances every 5 min, the entire past 30 min of orbit data are updated upon completion of each POD process. To properly validate the consistency of real-time processing, only the portion covered by the new 5-min data is included in the comparison. Fig. 5 illustrates the orbital differences between the reference orbit and the POD results based on CODE final products in radial (R), along-track (T), and cross-track (N) directions for all satellites according to our comparison strategy. Table 4 summarizes the statistics of these differences. The data from the initial three hours are excluded during the analysis, avoiding the impact of non-converged results on the statistical results.

As shown in Fig. 5 and Table 4, all satellites achieve centimeter-level POD consistency. S6MF achieves the highest consistency in both radial and 3D directions, with values of 2.14 cm and 4.36 cm, respectively. This is attributed to its high altitude which minimize the effects of gravity and drag forces on orbit determination, and state-of-the-art GNSS receiver ensuring high-quality GNSS observations(Montenbruck et al., 2021). SE3B follows closely behind, with radial and 3D RMS values of 2.55 cm and 4.45 cm, respectively.

In contrast, SWMA was launched in 2013 (seven years before S6MF) and has a much lower altitude, making its orbit more sensitive to atmospheric drag and high-degree gravity field perturbations. Consequently, it exhibits rela-

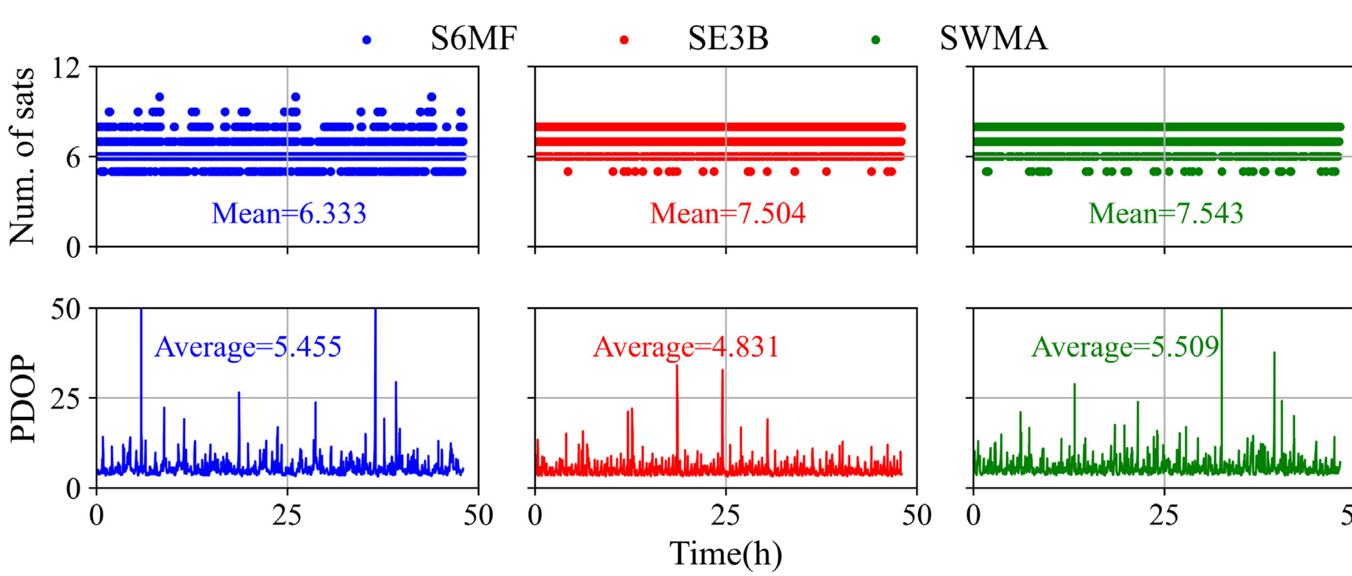

Fig. 4. The number of satellites and PDOP for S6MF, SE3B and SWMA.

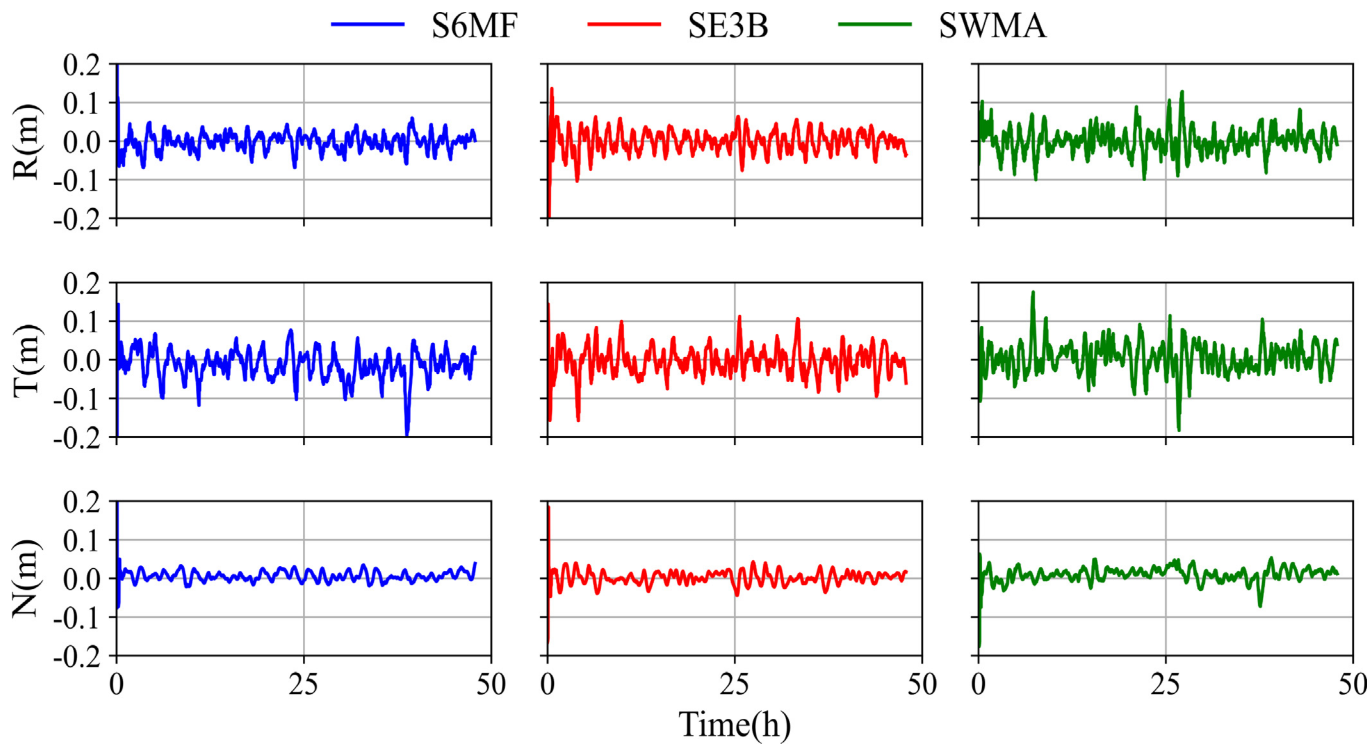

Fig. 5. The orbital difference between the reference orbit and POD results based on CODE final products (considering the updating parts only) in radial (R), along-track (T) and cross-track (N) directions for S6MF, SE3B and SWMA.

Table 4
Statistics of the orbital difference between the reference orbit and POD results based on CODE final products (considering the updating parts only) for S6MF, SE3B and SWMA (unit: cm).

Satellite	Radial Mean ± RMS	Along-track Mean ± RMS	Cross-track Mean ± RMS	3D-RMS
S6MF	-0.07 ± 2.14	-1.44 ± 3.62	0.64 ± 1.15	4.36
SE3B	-0.00 ± 2.55	-0.33 ± 3.34	0.19 ± 1.47	4.45
SWMA	0.11 ± 3.02	0.56 ± 3.70	1.08 ± 1.64	5.05

tively lower consistency, with values of 3.02 cm and 5.05 cm in the radial and 3D directions, respectively.

5.2. Orbital prediction performance in user arc

According to our orbit determination strategy, orbital prediction is performed immediately after completing the POD of each arc, and the part within the user arc is sent to the user. Therefore, this section primarily focuses on validating the consistency of the data within the user arc.

After processing all arcs, we obtain a total of 556 user arcs, with each user arc containing 20 min of predicted orbits. For convenience, we slice the data of each user arc by minute and then combine them for statistical analysis to evaluate the orbit prediction consistency. Fig. 6 presents the minute-wise box plots of orbital differences between the reference orbit and the sliced orbital predictions in the R, T, and N directions for the three satellites. Table 5 summarizes the statistics of these differences at typical time points of 10 min and 20 min.

According to Fig. 6 and Table 5, due to the different POD consistency and orbital altitudes, all three satellites exhibit varying degrees of orbit consistency degradation as prediction time increases. However, within the user arc, they all maintain an average 3D RMS of orbit prediction consistency better than 20 cm.

SWMA has the lowest POD consistency and the lowest orbital altitude, so its orbit consistency degrades the fastest. At the 10th minute within the user arc, the 3D-RMS is 11.39 cm, and it can maintain RMS values better than 10 cm in all RTN directions. But at the 20th minute, the 3D-RMS degrades to 16.80 cm. Especially in T direction, which degrades to 15.23 cm, and in some arc segments, it even exceeds 60 cm.

S6MF has the highest POD consistency and the highest orbital altitude. Thus, the consistency degradation of its predicted orbit is the slowest. It can maintain an RMS value better than 10 cm in all RTN directions within the user arc. At the 20th minute within the user arc, the 3D-RMS is 9.42 cm, better than 10 cm.

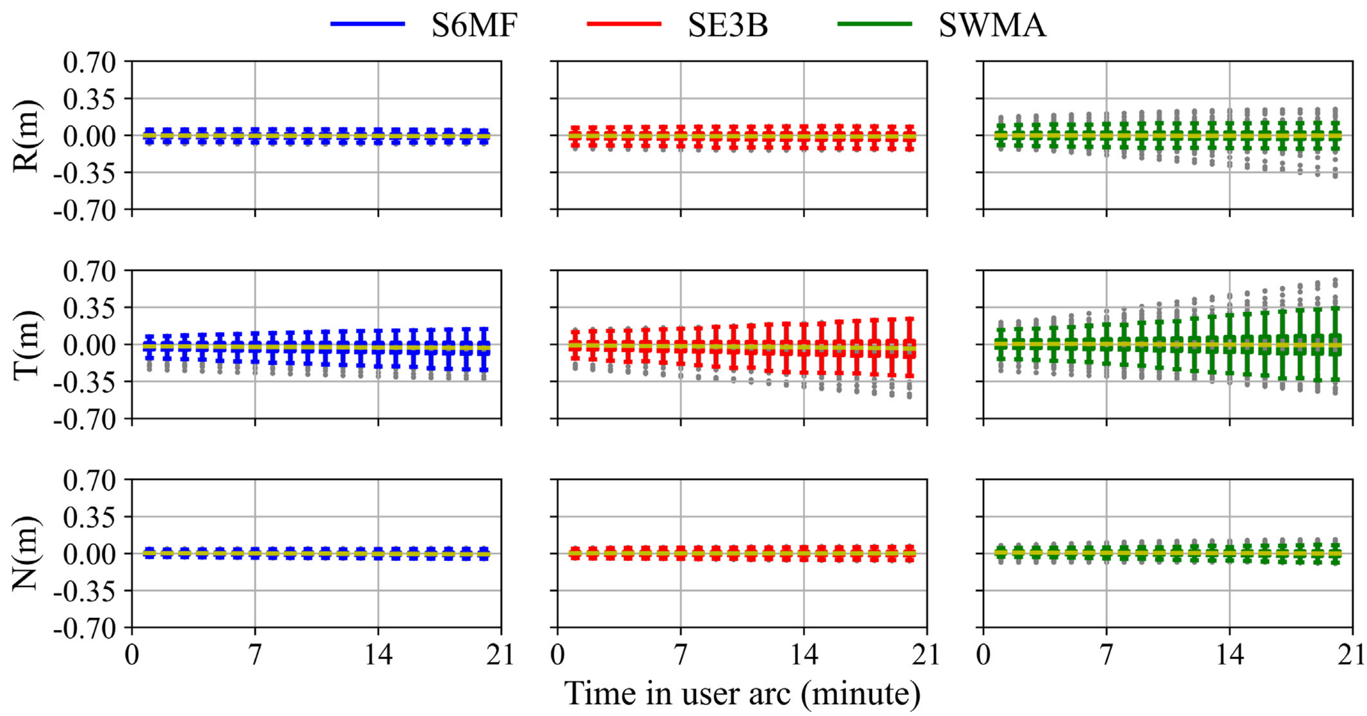

Fig. 6. The minute-wise box-plot of orbital difference between the reference orbit and orbital prediction (merged by 556 user arcs' data) in radial (R), along-track (T) and cross-track (N) directions for S6MF, SE3B and SWMA.

Table 5
Statistics of the orbital difference between the reference orbit and orbital prediction (merged by 556 user arcs' data) at 10 and 20 min for S6MF, SE3B and SWMA.

Satellite	Direction	Time in user arc	Peak value	Mean ± STD	RMS
S6MF	R	10 min	−8.41 cm	−0.60 ± 2.47 cm	2.54 cm
		20 min	−8.15 cm	−0.80 ± 2.33 cm	2.47 cm
	T	10 min	−28.43 cm	−3.03 ± 5.96 cm	6.69 cm
		20 min	−32.66 cm	−4.27 ± 7.65 cm	8.88 cm
	N	10 min	4.60 cm	−0.00 ± 1.60 cm	1.60 cm
		20 min	−5.07 cm	−0.43 ± 1.90 cm	1.95 cm
	3D	10 min	—	—	7.33 cm
		20 min	—	—	9.42 cm
SE3B	R	10 min	−14.11 cm	−0.84 ± 3.75 cm	3.84 cm
		20 min	−13.62 cm	−1.09 ± 3.99 cm	4.13 cm
	T	10 min	−34.32 cm	−2.54 ± 7.72 cm	8.12 cm
		20 min	−49.51 cm	−4.38 ± 11.06 cm	11.90 cm
	N	10 min	6.18 cm	0.05 ± 2.15 cm	2.15 cm
		20 min	−7.09 cm	0.03 ± 2.54 cm	2.54 cm
	3D	10 min	—	—	9.23 cm
		20 min	—	—	12.85 cm
SWMA	R	10 min	−22.81 cm	−0.19 ± 5.28 cm	5.29 cm
		20 min	−38.74 cm	−0.52 ± 6.24 cm	6.26 cm
	T	10 min	38.07 cm	0.12 ± 9.73 cm	9.74 cm
		20 min	60.90 cm	−0.50 ± 15.22 cm	15.23 cm
	N	10 min	11.50 cm	0.48 ± 2.57 cm	2.61 cm
		20 min	13.06 cm	−0.16 ± 3.32 cm	3.32 cm
	3D	10 min	—	—	11.39 cm
		20 min	—	—	16.80 cm

Table 6
Projection factors for S6MF, SE3B and SWMA.

	S6MF	SE3B	SWMA
w_R	0.6045	0.5064	0.4170
$w_{T,N}$	0.3160	0.3706	0.4122

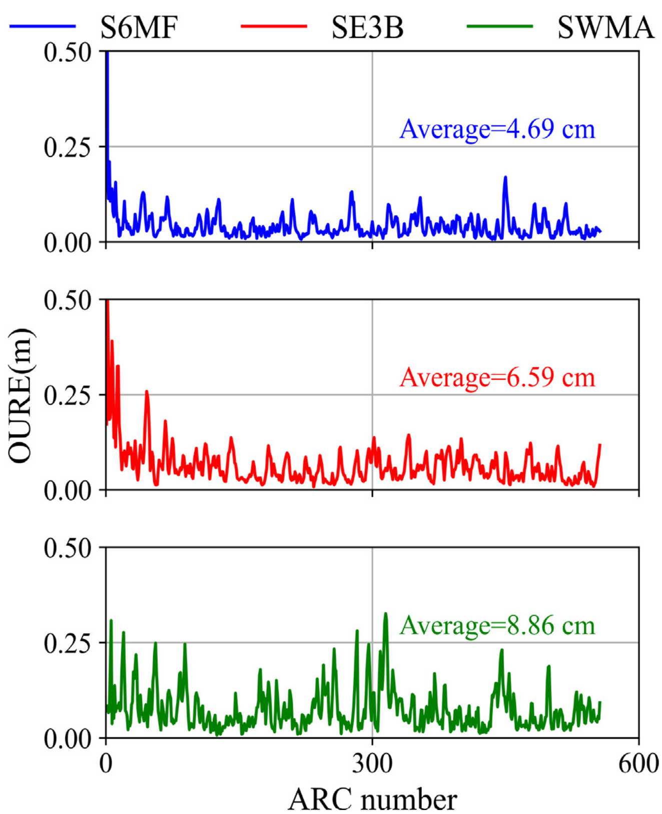

Fig. 7. The OURE of each user arc for S6MF, SE3B and SWMA, and the number in the figure represents the average OURE.

SE3B achieves a POD consistency comparable to that of S6MF. However, due to its lower orbital altitude, it is more affected by the Earth's gravitational force and atmospheric drag, and its orbit degradation is faster than that of S6MF. At the 10th minute within the user arc, it can maintain an RMS value better than 10 cm in all three RTN directions, and with a 3D RMS of 9.23 cm. But by the 20th minute, the RMS value in the T direction degrades to 11.90 cm, and the 3D RMS value degrades to 12.85 cm.

As the prediction orbit within user arc is mainly used to fit BRDC, the orbital user range error (OURE)(Wang et al., 2022) is used to validate the consistency of our orbital prediction results in providing navigation services to ground users. The equation to calculate the OURE is written as:

$$\sigma_{OURE} = \sqrt{w_R\sigma_R^2 + w_{T,N}(\sigma_T^2 + \sigma_N^2)} \tag{30}$$

where σ_R^2, σ_T^2 and σ_N^2 denote the Root Mean Square Error (RMSE) of the orbit in radial, along- and cross-track directions, respectively. w_R and $w_{T,N}$ denote the projection factors, they are mainly determined by the orbital altitude (Chen et al., 2013). The projection factors of these three satellites are liste in Table 6.

Fig. 7 shows the OURE of each user arc for these three satellites. As shown in Fig. 7, S6MF has the smallest average OURE reaching 4.69 cm. This is related to its highest orbit prediction consistency, especially in R direction. Since S6MF operates at a relatively high orbital altitude, Eq. (30) indicates that radial consistency contributes the most significantly to OURE. For SE3B, which has a slightly lower orbital altitude compared to S6MF, the contributions of the T and N directions to the OURE are increased. Moreover, the significant degradation of the orbit consistency in the T direction results in an increase in average OURE of SE3B to 6.59 cm compared to S6MF. SWMA has the largest average OURE at 8.86 cm, as its large degradation of orbit prediction consistency and lower orbital altitude cause nearly equal contributions from the R, T, and N directions to the OURE. Overall, the average OURE values for all three satellites remain below 10 cm.

It should be noted that due to calculation delays, for each user arc, the stored prediction orbit covers a duration of 20 min, starting from the 5-min of all the prediction results. This means that the 10th minute within the user arc corresponds to the 15th minute of orbit prediction, and similarly, the 20th minute within the user arc corresponds to the 25th minute of orbit prediction.

5.3. POD performance based on GNSS broadcast ephemerides

In some scenarios, LEO satellites can only use the broadcast ephemerides transmitted by GNSS for RTPOD. Therefore, it is necessary to validate the POD & orbital prediction performance of our processing strategy under this scenario.

Fig. 8 shows the orbital differences between the reference orbit and POD results based on GNSS broadcast ephemerides in R, T and N directions of each satellite. Meanwhile, Table 7 presents a statistical analysis of these differences.

According to Fig. 8 and Table 7, the POD consistency of the S6MF satellite based on GNSS broadcast ephemerides is the lowest among the three satellites, differing from the results obtained using CODE final products previously. Its 3D-RMS is 50.65 cm, while the corresponding values for SE3B and SWMA are 34.95 cm and 34.73 cm, respectively. The primary reason is that the Total Group Delay (TGD) in the broadcast ephemerides is not applied to correct the signal delays in the C1C and C2L observations of S6MF during the orbit determination process. Nevertheless, all three satellites achieve decimeter-level POD consistency, with SE3B and SWMA showing 3D RMS consistency better than 40 cm. This level of consistency sat-

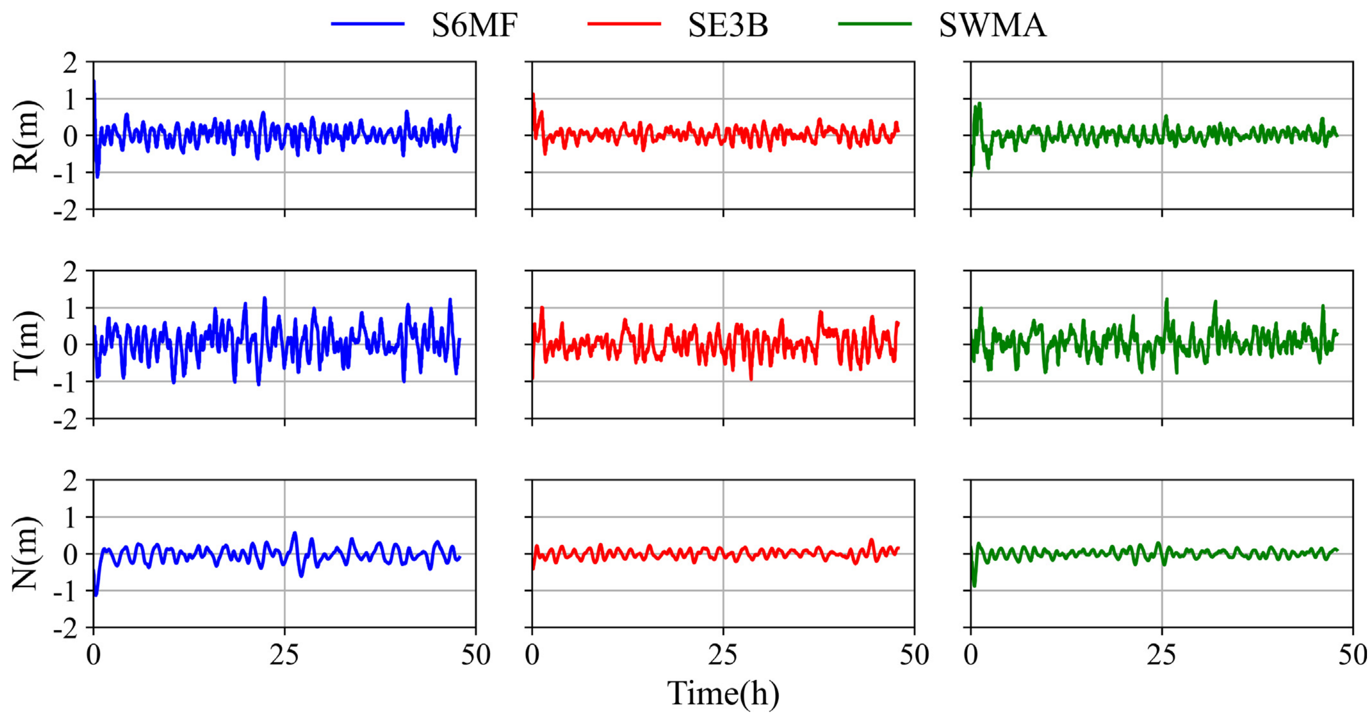

Fig. 8. The orbital difference between the reference orbit and POD results based on GNSS broadcast ephemerides (considering the updating parts only) in radial (R), along-track (T) and cross-track (N) directions for S6MF, SE3B and SWMA.

Table 7
Statistics of the orbital difference between the reference orbit and POD results based on GNSS broadcast ephemerides (considering the updating parts only) for S6MF, SE3B and SWMA (unit: cm).

Satellite	Radial Mean ± RMS	Along-track Mean ± RMS	Cross-track Mean ± RMS	3D-RMS
S6MF	-1.51 ± 23.28	6.12 ± 40.98	-1.95 ± 18.66	50.65
SE3B	0.15 ± 15.75	1.30 ± 29.24	1.80 ± 10.86	34.95
SWMA	0.15 ± 15.10	1.29 ± 29.68	0.46 ± 9.89	34.73

isfies most requirements for RT or NRT orbit consistency at the 1-m level.

We also obtained 556 user arcs for each satellite in this scenario. The orbital differences between the predicted and reference orbits were statistically analyzed at the 10th and 20th minutes of the user arc, as summarized in Table 8.

Compared with the results obtained using CODE final products, the prediction orbits of this scenario shows a clear degradation, mainly in the along-track direction. Nevertheless, the predicted orbits remain at the decimeter- to meter-level. The 3D RMS values at the 10th and 20th minutes are 0.77 m and 0.91 m for S6MF, 0.57 m and 0.66 m for SE3B, and 0.56 m and 0.66 m for SWMA, respectively. These results indicate that, although this scenario is insufficient for high-precision applications such as LEO-PNT, InSAR, or satellite altimetry, the proposed strategy can still provide useful orbit products for LEO onboard autonomous orbit determination and applications with meter-level orbit requirements, such as some optical remote sensing missions, depending on their specific orbit accuracy requirements.

6. Conclusions

Emerging LEO navigation constellations require not only real-time positioning but also the capability to generate high-precision prediction orbits. To address the conflict between the need for dynamic fitting and the constraints of onboard computing resources, we formulated the sequential least squares into an onboard adaptive sequential filtering strategy. Unlike traditional batch processing, this strategy utilizes a sliding window to directly provide fast and stable prediction orbits immediately after the POD of each arc is completed.

To simulate real-time processing and validate the performance of this strategy, we used spaceborne GNSS data from three satellites at typical orbital altitudes: Sentinel-6 Michael Freilich (S6MF), Sentinel-3B (SE3B), and

Table 8
Statistics of the orbital difference between the predicted and reference orbits (merged by 556 user arcs' data) at 10 and 20 min for S6MF, SE3B and SWMA.

Satellite	Direction	Time in user arc	Peak value	Mean ± STD	RMS
S6MF	R	10 min	0.68 m	0.01 ± 0.23 m	0.23 m
		20 min	0.63 m	0.00 ± 0.20 m	0.20 m
	T	10 min	−2.02 m	0.07 ± 0.70 m	0.70 m
		20 min	−2.47 m	0.07 ± 0.85 m	0.86 m
	N	10 min	−0.62 m	0.00 ± 0.19 m	0.19 m
		20 min	−0.62 m	0.02 ± 0.20 m	0.20 m
	3D	10 min	—	—	0.77 m
		20 min	—	—	0.91 m
SE3B	R	10 min	0.45 m	0.01 ± 0.15 m	0.15 m
		20 min	0.41 m	0.01 ± 0.12 m	0.13 m
	T	10 min	1.53 m	0.03 ± 0.53 m	0.53 m
		20 min	1.82 m	0.03 ± 0.63 m	0.63 m
	N	10 min	−0.30 m	0.01 ± 0.11 m	0.11 m
		20 min	−0.35 m	0.01 ± 0.11 m	0.11 m
	3D	10 min	—	—	0.57 m
		20 min	—	—	0.66 m
SWMA	R	10 min	−0.49 m	−0.01 ± 0.15 m	0.15 m
		20 min	−0.79 m	−0.03 ± 0.14 m	0.14 m
	T	10 min	2.00 m	0.04 ± 0.52 m	0.52 m
		20 min	2.31 m	0.01 ± 0.62 m	0.62 m
	N	10 min	0.33 m	0.01 ± 0.10 m	0.10 m
		20 min	0.38 m	0.01 ± 0.11 m	0.11 m
	3D	10 min	—	—	0.56 m
		20 min	—	—	0.66 m

Swarm-A (SWMA), and evaluated the results against independent precise reference orbits.

With the support of high-precision GNSS products, this strategy achieves centimeter-level POD consistency. Specifically, the radial RMS values of S6MF and SE3B are better than 3 cm, and the 3D RMS values are better than 5 cm, demonstrating the effectiveness of the adaptive filtering strategy.

Crucially for navigation services, the strategy delivers stable short-term predictions. The 15-min orbit prediction, corresponding to the 10th minute of the user arc, achieves 3D RMS consistency better than 15 cm, with S6MF and SE3B remaining below 10 cm. The 25-min orbit prediction, corresponding to the 20th minute of the user arc, achieves 3D RMS consistency better than 20 cm, with S6MF maintaining consistency within 10 cm. Furthermore, the navigation service capability for ground users is evaluated through the Orbital User Range Error (OURE), yielding average values of 4.69 cm, 6.59 cm, and 8.86 cm for S6MF, SE3B, and SWMA, respectively.

In scenario limited to GNSS broadcast ephemerides, this strategy maintains decimeter-level POD consistency, with 3D RMS values of 50.65 cm, 34.95 cm, and 34.73 cm for S6MF, SE3B, and SWMA, respectively. The corresponding short-term prediction consistency degrades to the decimeter- to meter-level. At the 20th minute of the user arc, the 3D RMS values are 0.91 m, 0.66 m, and 0.66 m for S6MF, SE3B, and SWMA, respectively. These results indicate that the BRDC-only case is insufficient for high-precision LEO-PNT BRDC generation, but it can still provide useful orbit products for onboard autonomous orbit determination and meter-level LEO applications.

Declaration of competing interest

The authors declare the following financial interests/personal relationships which may be considered as potential competing interests:[Yezhi Song reports financial support was provided by Shanghai Astronomical Observatory, Chinese Academy of Sciences. If there are other authors, they declare that they have no known competing financial interests or personal relationships that could have appeared to influence the work reported in this paper.].

Acknowledgments

This research was funded by the National Key R&D Program of China (2025YFF0511200). We would like to acknowledge Prof. Maorong Ge for his invaluable guidance and constructive suggestions during the early stages of this work. We equally would like to acknowledge Dr. Jianfeng Cao for providing practical references that greatly benefited the development of our software. We also would like to acknowledge Copernicus Data Space Ecosystem and ESA for providing Sentinel-6 MF, Sentinel-3B and Swarm-A data. Finally, we appreciate the reviewers and editors' valuable comment to improve the paper quality.

References

Beutler, G., Brockmann, E., Hugentobler, U., et al., 1996. Combining consecutive short arcs into long arcs for precise and efficient GPS Orbit Determination. J. Geod. 70, 287–299. https://doi.org/10.1007/BF00867349.

Chen, J., Wang, J., Yu, C., et al., 2022. Improving BDS broadcast ephemeris accuracy using ground-satellite-link observations. Satell. Navig. 3 (1), 11. https://doi.org/10.1186/s43020-022-00072-4.

Chen, L., Jiao, W., Huang, X. et al., 2013. Study on Signal-In-Space Errors Calculation Method and Statistical Characterization of BeiDou Navigation Satellite System. In J. Sun, W. Jiao, H. Wu, & C. Shi (Eds.), China Satellite Navigation Conference (CSNC) 2013 Proceedings (pp. 423–434). Berlin, Heidelberg: Springer, Berlin Heidelberg volume 243. doi:10.1007/978-3-642-37398-5_39.

Fernández, J., Peter, H., Fernández, C., et al., 2024. The Copernicus POD Service. Adv. Space Res. 74 (6), 2615–2648. https://doi.org/10.1016/j.asr.2024.02.056.

Fernández, M., Peter, H., Arnold, D., et al., 2022. Copernicus Sentinel–1 POD reprocessing campaign. Adv. Space Res. 70 (2), 249–267. https://doi.org/10.1016/j.asr.2022.04.036.

Folkner, W.M., Williams, J.G., Boggs, D.H., 2009. The planetary and lunar ephemeris DE 421. Interplanet. Netw. Prog. Rep., 42–178

Förste, C., Flechtner, F., Schmidt, R. et al., 2006. A mean global gravity field model from the combination of satellite mission and altimetry/gravimetry surface gravity data. In: Poster Presented at EGU General Assembly 2006 (p. 03462). Vienna, Austria: Geophysical Research Abstracts volume 8.

Fu, W., Huang, G., Zhang, Q., et al., 2019. Multi-GNSS real-time clock estimation using sequential least square adjustment with online quality control. J. Geod. 93 (7), 963–976. https://doi.org/10.1007/s00190-018-1218-z.

Ge, M., Gendt, G., Dick, G., et al., 2006. A New Data Processing Strategy for Huge GNSS Global Networks. J. Geod. 80 (4), 199–203. https://doi.org/10.1007/s00190-006-0044-x.

Jin, S., Gao, C., Yuan, L., et al., 2021. Long-term variations of plasmaspheric total electron content from topside GPS observations on LEO Satellites. Remote Sens. 13 (4), 545. https://doi.org/10.3390/rs13040545.

Kunzi, F., Montenbruck, O., Perazzetti, F., 2026. Gnss-based real-time orbit determination and prediction for leo-pnt ephemeris generation. Adv. Space Res. 77 (1), 923–938. https://doi.org/10.1016/j.asr.2025.11.082.

Laniewski, D., Lanfer, E., Aschenbruck, N., 2025. Measuring mobile starlink performance: a comprehensive look. IEEE Open J. Commun. Soc. 6, 1266–1283. https://doi.org/10.1109/OJCOMS.2025.3539836.

Li, X., 2024. LEO real-time ambiguity-fixed precise orbit determination with onboard GPS/Galileo observations. GPS Solut. 28 (188). https://doi.org/10.1007/s10291-024-01729-0.

Li, X., Chen, X., Ge, M., et al., 2019. Improving multi-GNSS ultra-rapid orbit determination for real-time precise point positioning. J. Geod. 93 (1), 45–64. https://doi.org/10.1007/s00190-018-1138-y.

Liao, M., Tang, C., Zhou, S., et al., 2024. Efficiency optimization method of precise orbit determination for navigation satellites based on domestic ARM Architecture CPU. J. Geod. Geodyn. 44 (04), 366–371.

Lyard, F., Lefevre, F., Letellier, T., et al., 2006. Modelling the global ocean tides: Modern insights from FES2004. Ocean Dyn. 56 (5–6), 394–415. https://doi.org/10.1007/s10236-006-0086-x.

Mao, X., Wang, W., Gao, Y., 2024. Precise orbit determination for low Earth orbit satellites using GNSS: Observations, models, and methods. Astrodynamics. https://doi.org/10.1007/s42064-023-0195-z.

Mao, Y., Hu, X., Song, X., et al., 2015. Satellite autonomous navigation algorithm analysis based on broadcast ephemeris parameters. SCI. SIN. Phys. Mech. Astron. 45 (7). https://doi.org/10.1360/SSPMA2015-00126, 079512–079512.

Montenbruck, O., Hackel, S., Wermuth, M., et al., 2021. Sentinel-6A precise orbit determination using a combined GPS/Galileo receiver. J. Geod. 95 (9), 109. https://doi.org/10.1007/s00190-021-01563-z.

Montenbruck, O., Kunzi, F., Hauschild, A., 2022. Performance assessment of GNSS-based real-time navigation for the Sentinel-6 spacecraft. GPS Solut. 26 (1), 12. https://doi.org/10.1007/s10291-021-01198-9.

Montenbruck, O., Steigenberger, P., Hugentobler, U., 2015. Enhanced solar radiation pressure modeling for Galileo satellites. J. Geod. 89 (3), 283–297. https://doi.org/10.1007/s00190-014-0774-0.

Petit, G., Luzum, B., 2010. IERS conventions (2010). Tech. Rep. DTIC Document 36, 180.

Picone, J.M., Hedin, A.E., Drob, D.P., et al., 2002. NRLMSISE-00 empirical model of the atmosphere: Statistical comparisons and scientific issues. J. Geophys. Res.: Space Phys. 107 (A12). https://doi.org/10.1029/2002JA009430.

Tapley, B.D., Schutz, B.E., Born, G.H., 2004. Chapter 2 - the orbit problem. In: Statistical Orbit Determination. Academic Press, Burlington, pp. 17–91.

Wang, K., El-Mowafy, A., Yang, X., 2022. URE and URA for predicted LEO satellite orbits at different altitudes. Adv. Space Res. 70 (8), 2412–2423. https://doi.org/10.1016/j.asr.2022.08.039.

Wang, Z., Wang, L., Li, Z. et al. (2023). Real-time precise orbit determination for FY-3C and FY-3D based on BDS and GPS onboard observation. IET Radar Sonar Navig., (p. rsn2.12413). doi:10.1049/rsn2.12413.

Xiang, W., Zhang, R., Liu, G., et al., 2022. Extraction and analysis of saline soil deformation in the Qarhan Salt Lake region (in Qinghai, China) by the sentinel SBAS-InSAR technique. Geod. Geodyn. 13 (2), 127–137. https://doi.org/10.1016/j.geog.2020.11.003.

Yang, Y., Gao, W., 2006. An optimal adaptive kalman filter. J. Geod. 80 (4), 177–183. https://doi.org/10.1007/s00190-006-0041-0.

Yang, Y., Mao, Y., Ren, X., et al., 2024. Demand and key technology for a LEO constellation as augmentation of satellite navigation systems. Satell. Navig. 5 (1), 11. https://doi.org/10.1186/s43020-024-00133-w.

Yang, Y., Ren, X., Xu, Y., 2013. Main progress of adaptively robust filter with applications in navigation. J. Navig. Position. 1 (01), 9–15. https://doi.org/10.16547/j.cnki.10-1096.2013.01.006.

Zhang, Q., Liu, L., 1998. The comparison between Adams-Cowell method and KSG integrator. Publ. purple mt. obs. 01, 21–29.

Zhao, Q., Xu, X., Ma, H., et al., 2018. Real-Time Precise Orbit Determination of BDS/GNSS: Method and Service. Geomat. Inf. Sci. Wuhan Univ. 43 (12), 2157–2166. https://doi.org/10.13203/j.whugis20180374.